White Rose Research Online

eprints@whiterose.ac.uk
https://eprints.whiterose.ac.uk
Universities of Leeds, Sheffield and York

Deposited via The University of Sheffield.

White Rose Research Online URL for this paper:
https://eprints.whiterose.ac.uk/id/eprint/247318/

Version: Published Version

Article:
Rojas-Arques, S., Nichols, A. and Shucksmith, J.D. (2026) Transverse mixing and pollutant dispersion in open-channel flow with interacting vegetated shear layers. Environmental Fluid Mechanics, 26 (6). 51. ISSN: 1567-7419

https://doi.org/10.1007/s10652-026-10109-w

Reuse
This article is distributed under the terms of the Creative Commons Attribution (CC BY) licence. This licence allows you to distribute, remix, tweak, and build upon the work, even commercially, as long as you credit the authors for the original work. More information and the full terms of the licence here: https://creativecommons.org/licenses/

Takedown
If you consider content in White Rose Research Online to be in breach of UK law, please notify us by emailing eprints@whiterose.ac.uk including the URL of the record and the reason for the withdrawal request.

UNIVERSITY OF LEEDS
University of Sheffield
UNIVERSITY of York

Environmental Fluid Mechanics (2026) 26:51
https://doi.org/10.1007/s10652-026-10109-w

ORIGINAL ARTICLE

Transverse mixing and pollutant dispersion in open-channel flow with interacting vegetated shear layers

S. Rojas-Arques[1,2] · A. Nichols[2] · J. D. Shucksmith[2]

Received: 20 January 2026 / Accepted: 13 September 2026
© The Author(s) 2026

Abstract

Pollutant discharges from combined sewer overflows and wastewater treatment works can degrade river water quality, and their impact is strongly controlled by transverse mixing. Vegetated channel margins generate turbulent shear layers that can enhance this mixing, but the role of interacting shear layers produced by vegetation on both banks remains poorly quantified. This paper presents an extensive high-resolution laboratory dataset for single- and dual-bank emergent vegetation in shallow open-channel flow. Surface velocities and depth-averaged solute mixing were measured using large-scale particle image velocimetry and planar concentration analysis. A finite-difference solution of the advection-diffusion equation was used to infer transverse mixing coefficients. The datasets are used to develop bulk parameterisations linking vegetation projected area and the velocity contrast between vegetated and free flow regions to shear-layer structure and transverse mixing. For single-bank flows, the displacement of the velocity inflection point and the inner and outer shear-layer thicknesses collapse to simple functions of vegetation density. Additionally, the maximum transverse mixing coefficient scales with the product of water depth and velocity difference between the vegetated region and the free flow. For dual-bank configurations, new empirical relationships quantify the reduction of centreline velocity and the enhancement of transverse mixing as shear layers interact across the free flow gap. The resulting model reproduces measured velocity and concentration fields with coefficients of determination typically exceeding 0.9 using only bulk flow and vegetation properties. These parameterisations provide a practical tool for representing transverse mixing in numerical models and for assessing how vegetated banks influence pollutant dispersion in rivers.

Highlights

- Vegetation along channel banks strongly shapes how pollution spreads across the flow.
- Mixing increases when shear zones from both banks meet, helping dilute pollutants faster.
- Simple measures of flow and vegetation give reliable estimates of how quickly pollution will disperse.

Keywords Transverse mixing · Mixing layers · Shear effects · Vegetation · Dual bank vegetation

Extended author information available on the last page of the article

Published online: 21 October 2026

1 Introduction

The effective management of water resources is indispensable for activities such as potable water supply, irrigation and industry. However, societal trends such as population growth and urbanisation can lead to increased stress on water resources and river systems via over abstraction and increased pollution loadings from agriculture and industry [21, 28, 43, 45]. Mixing processes in surface waters have a significant effect on concentrations of pollutants from discharges such as wastewater treatment works and sewer overflows [2, 8], and hence understanding these processes is important for the management of water resources.

Aside from initial momentum and vertical mixing effects downstream of a pollutant discharge, transverse mixing is generally the dominant physical process affecting pollutant concentrations at length scales up to approximately 300 times the channel width [37]. Improved understanding and enhancement of these processes to rapidly reduce peak concentrations may therefore offer a method to reduce the local impact of pollutant discharges. Existing studies considering the enhancement of transverse mixing have focused on the use of manufactured vanes [1, 38], whilst numerous other studies have shown how increased secondary currents (e.g., at confluences or in compound channels) can increase transverse mixing [4, 11].

Vegetated zones may also affect local transverse mixing rates by increasing velocity gradients and turbulent diffusion across the vertical water/vegetation interface, creating a shear layer over the horizontal plane [48, 49], as well as the potential enhancement of secondary currents. In the shear region, transport is dominated by the presence of large-scale coherent flow structures, and mixing can be characterised by the properties of the shear layer itself [10]. The interaction of vegetation properties, coherent flow structures and momentum transport at such interfaces has been studied by Caroppi et al., [3], who considered the significance of vegetation morphology on the properties of the shear layer. Liu et al., [16] developed an exponential-based model for predicting velocity fields in partially vegetated channels containing finite vegetation patches located either centrally or along one side of the channel. Their work demonstrated how vegetation drag produces strong lateral velocity gradients and distinct flow regions within and outside the patch, and provided a predictive framework for the resulting depth-averaged velocity field.

The effects of vegetation induced horizontal shear layers on mixing were considered by West et al., [47], who produced a modelling framework to describe the evolution of solute concentrations across a shear layer in a partially vegetated channel. Transverse mixing coefficients under such layers are highly heterogeneous, being enhanced within the shear layer but potentially reduced within the vegetation itself, relative to the main channel, due to the reduction in turbulent length scales caused by the vegetation stems [5, 23].

In many open-channel flows, vegetation occurs in patches or along one or both river banks, often leaving relatively narrow regions of unobstructed flow. Previous studies of mixing within vegetated shear layers have, however, focused primarily on configurations with a single vegetated bank or isolated vegetation patches [18–20, 33, 46–49, 51]. While such configurations are highly relevant, they differ fundamentally from bank-attached vegetation that generates laterally developing shear layers, particularly for channels with vegetation on both banks where opposing shear layers may interact across the channel width. Consequently, models developed for isolated patches are not directly applicable to flows featuring interacting vegetated banks.

Previous studies concerning interacting shear layers have focused mainly on the case of compound channels featuring vegetation [6, 7]. These studies confirm the presence of large-scale coherent structures and secondary currents within the main channel, but did not investigate mass transport. The interaction of shear layers, and effects on mixing, caused by banks on either side of the channel width has not yet been extensively studied.

Resolving the coupled velocity and transport processes associated with interacting shear layers requires spatially distributed observations of flow behaviour across large domains, which are difficult to obtain using conventional intrusive instrumentation in shallow free-surface environments. Advances in non-intrusive, mobile and distributed measurement techniques have improved the ability to characterise such flows while minimising disturbance to the flow field [15, 26, 27, 34].

This paper aims to utilise an experimental study of mixing processes in artificial vegetation to propose analytical relationships between vegetation properties, velocity profiles and the resulting transverse mixing rates in open channel flows featuring both single and dual vegetated banks. The work develops and tests new empirical relationships linking vegetation properties, shear-layer structure, and transverse mixing. The outcome is a simplified predictive framework that can estimate velocity and mixing characteristics in vegetated channels based solely on bulk flow and vegetation parameters, providing a foundation for future analytical and numerical model development. For simplicity, in this case, realistic flexible vegetation types are not considered in this work.

The paper is structured as follows. Section 2 reviews the background on vegetated shear layers and existing models for velocity and transverse mixing. Section 3 describes the experimental setup, vegetation configuration, Large-Scale Particle Image Velocimetry (LSPIV) and Planar Concentration Analysis (PCA) measurements, and the finite-difference mixing model. Section 4 presents new parameterisations of the streamwise velocity profile for single- and dual-bank configurations, derived by combining the present dataset with those of White and Nepf [46, 48, 49]. Section 5 then uses these velocity parameterisations to construct and test a bulk transverse-mixing relationship based on the maximum mixing coefficient $D_{y_{max}}$, first for single-bank flows and then for dual-bank cases with interacting shear layers. Section 6 discusses the implications of these results, compares them with previous studies, and outlines limitations and directions for future work, while Sect. 7 summarises the main conclusions.

2 Background

Vegetated shear layers generated over the vertical plane, commonly by flow over submerged vegetation, have been extensively studied (e.g., [13, 29, 32]). Reduced velocities due to vegetated drag in the region close to the bed result in high velocity gradients and turbulent intensities around the vegetation/free flow interface, with the point of maximum Reynolds stress and a corresponding inflection in the profile of streamwise velocity occurring at or near to the vegetation boundary. Ghisalberti and Nepf, [10] and Rubol et al., [36] studied vertical mixing within the shear layer in submerged vegetated flows, showing that vertical mixing can be characterised by the properties of the shear layer, and that flow over dense vegetation can result in rapid decreases of peak concentrations due to enhanced mixing. Horizontal shear layers generated by a vegetated bank have received comparatively less

attention, despite the increased complexity generated by the influence of the bed on the resulting flow structures at the interface [25]. White and Nepf, [48, 49] conducted a detailed study of the flow structure and profiles of streamwise velocities across a shear layer generated using rigid artificial vegetation, producing relationships for characteristic length scales (Fig. 1). White and Nepf, [48] defined the inner layer (of thickness δ_{Inner}) as the region of the shear layer between the inflection point (y_o) in the transverse profile of streamwise velocity and the region within the vegetation where the streamwise velocity becomes uniform. This region was considered equivalent to the penetration of the coherent structures generated within the shear layer into the vegetation. The outer layer (of thickness δ_{Outer}) is defined as the region of the shear layer between the inflection point (y_o) in the transverse profile streamwise velocity and the region within the free flow where the streamwise velocity becomes uniform. This was found to be related with the size of the large-scale eddies generated within the shear layer. No strong influence was found between the length of the outer region and the vegetation density, however White and Nepf [49] showed that δ_{Outer} is typically around ten times larger than δ_{Inner}. Based on their experimental results, White and Nepf , [49] proposed expressions to define length scales of the inner layer (δ_{Inner}) based on the obtaining of empirical coefficients, and depth-averaged profiles of streamwise velocity within the inner and outer layers. The profile of streamwise velocity within the inner shear layer (U_{Inner}) was considered as a hyperbolic tangent shear profile.

$$U_{Inner} = U_{Veg} + U_S \left(1 + tanh\left(\frac{y - y_o}{\delta_{Inner}}\right)\right) \tag{1}$$

where U_S is slip velocity, defined as $U_S = U(y_o) - U_{Veg}$ and determined via regression to experimental data. U_{Veg} is the depth averaged velocity in the vegetation (commonly evaluated by considering the drag resistance of an array of vegetation e.g. Jordanova et al., [14].

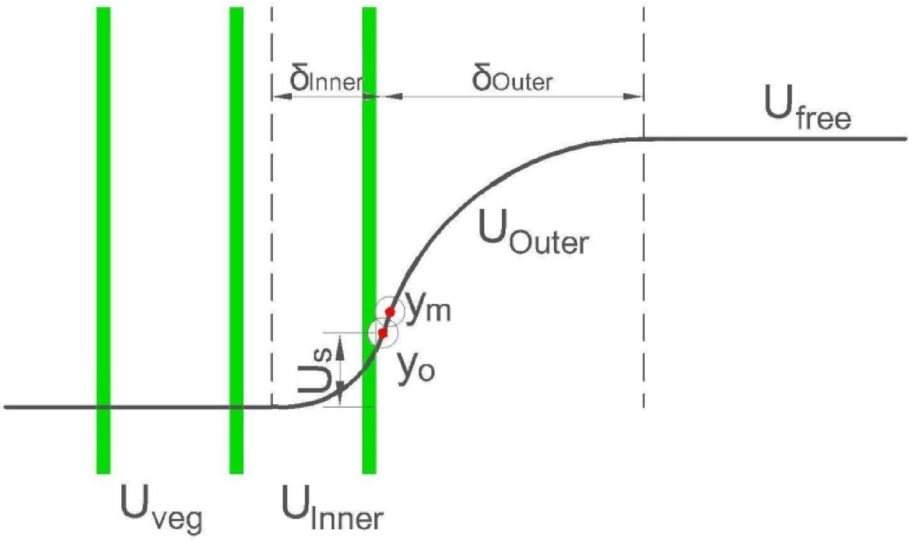


Fig. 1 Scheme describing the profile of streamwise velocity in a partially vegetated channel adapted from White and Nepf [49]. Note that y_0 is the inflection point in the transverse profile of streamwise velocity, while y_m is the point at which the gradient of Eq. 1 matches that of Eq. 2

The profile of streamwise velocity within the outer shear layer (U_{Outer}) was considered as a balance between the pressure gradient and the surface slope assuming a constant eddy viscosity.

$$U_{Outer} = U_m + (U_{Free} - U_m)\left[\frac{y - y_m}{\delta_{Outer}} - \frac{1}{4}\left(\frac{y - y_m}{\delta_{Outer}}\right)^2\right] \quad (2)$$

where y_m is the model matching point at which the inner and outer velocity profiles are joined with matching gradients and $U_m = U_{Outer}(y_m)$. U_{Free} is the depth averaged velocity of the free flow region, commonly evaluated using Manning's or Darcy-Weisbach equations (Fig. 1).

Beyond this framework, Tang et al., [41, 42] extended the classical Shiono and Knight [39] method to predict the lateral distribution of depth averaged velocity in partially vegetated channels. Their analytical solution to the depth-integrated Reynolds-averaged Navier–Stokes equation incorporates vegetation drag as a momentum-sink term and accounts for bed friction, lateral turbulence, and secondary flows. This work provides a theoretical basis for predicting velocity profiles in compound and vegetated channels, although it requires specification of several empirical coefficients (bed friction, lateral eddy viscosity, secondary flow, vegetation drag).

In addition, White and Nepf [49] showed that in banks with lower vegetation densities, i.e. $a \leq 3.9\,m^{-1}$ where a was defined as the mean projected area per unit volume $a = nd$, d is the stem diameter and n is the number of stems per unit area; the inflection point and the position of maximum Reynolds stress are displaced away from the interface point by a distance of $2d$. This displacement was also noticed by Meftah and Mossa [18, 19] for sparse vegetation densities. West et al., [47] conducted experiments using both artificial and real vegetation to study the variable profile of transverse mixing coefficient in partially vegetated flows. A Finite Difference Model (FDM) was used to solve the Advection-Diffusion Equation (ADE) for a steady-source and vertically well-mixed condition.

$$U(y)\,h(y)\frac{\partial C(x,y)}{\partial x} = \frac{\partial}{\partial y}\left[h(y)\,D_y(y)\frac{\partial C(x,y)}{\partial y}\right] \quad (3)$$

where D_y is the transverse mixing coefficient, h is the water depth, x is the lengthwise coordinate, y is the spanwise coordinate and C is the solute concentration. West et al., [47] proposed both continuous (semi-Gaussian) and stepped distributions of transverse mixing coefficient over the shear layer region, and the parameterisation of the distribution properties was performed using the measured profiles of streamwise velocity by optimising the fit between measured and predicted concentration profiles using Eq. 3. This resulted in five parameters for the continuous distribution and two for the simpler step distribution. The model was found to give a good representation of mixing processes across the water/vegetation interface using both the continuous and step distributions, however considerable variability was observed in the resulting parameters needed to describe the distribution.

Further work is therefore needed to better characterise transverse mixing across vegetated shear layers and to relate velocity profiles and mixing behaviour to easily measurable

flow and vegetation properties. The experiments described below were designed to address this need for both single and dual vegetated bank configurations.

3 Methodology

Experiments were conducted in the hydraulic laboratory of the University of Sheffield, within a flume of working length $14.5\,m$ and width $1.2\,m$, set at a fixed bed slope of $S_o = 0.00123$. Vegetation was simulated using artificial plastic cylinders with a stem diameter $d = 0.005\,m$ arranged in a staggered configuration, similar to those used in Hirschowitz and James [12] and in White and Nepf [49]. The height of the cylinders exceeded the water depth in all cases (i.e. emergent conditions). Uniform flow conditions were achieved by controlling both the tailgate weir at the downstream end of the channel and the flow rate valve until the same water depth was achieved within the entire measurement area (see Fig. 2). Uniform flow in the measurement area was verified from constant depth and surface velocity over the 4.48 m window. The vegetated bank extended continuously from the upstream baffle to the downstream tailgate, providing a sufficiently long vegetated reach for flow development consistent with previous studies [48, 49]. The water depth was measured using Vernier gauges with accuracy of 0.1 mm, installed 0.25 m upstream of the measurement area, 0.25 m downstream of the measurement area, and at the midpoint of the measurement area. A flow baffle was installed at the upstream end of the channel to dissipate turbulent structures produced during the flow injection.

An initial set of experiments was conducted with a single vegetated bank of width 0.42 m along the full length of the channel from the flow baffle to the flume tailgate (Fig. 2a). The 4.48 m long measurement area was situated 6 m downstream of the flow baffle to allow for a fully developed shear layer to be produced, in line with previous researchers with similar flow conditions [48, 49]. The vegetated width was designed to allow the full development of both inner and outer layers within shear layer according to the experimental results and the relationships proposed in White and Nepf ([48], [49]). Each flow condition was maintained under steady-state conditions, and repeat measurements were conducted for selected tests to verify the reproducibility of the velocity and concentration fields, showing negligible variation between runs.

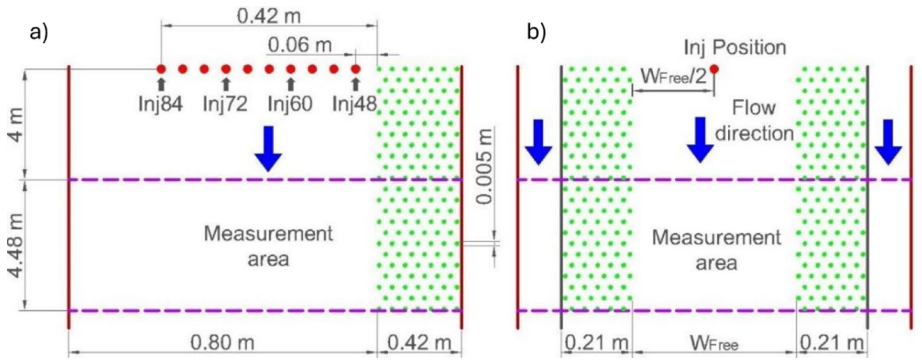


Fig. 2 Test setups for **a**) single vegetated bank and **b**) dual vegetated banks

Three different vegetation bank densities were considered with $a = 6.349\ m^{-1}$, $1.587\ m^{-1}$ and $0.397\ m^{-1}$. For each density, the vegetation consisted of a uniformly spaced, staggered array of cylindrical stems extending continuously along the length of the flume. The corresponding streamwise spacing between successive rows of stems was $x_{stem} = 0.0525\ m$, $0.1050\ m$ and $0.21\ m$; with a spanwise spacing between stems in each row of $y_{stem} = 0.03$ m, $0.06\ m$ and $0.12\ m$ for each vegetation density respectively. Moreover, for each vegetation density four different uniform flow depths were tested with $h = 0.036\ m$, $0.054\ m$, $0.072\ m$ and $0.090\ m$, obtaining a total of 12 different flow conditions (Table 1).

Based on results from this configuration, a second set of experiments was designed to study interacting shear layers with dual banks of vegetation separated by a free flow region of varying widths (W_{Free}) under the same vegetation densities and uniform flow depths. To keep approximately equivalent depth/discharge relationships within the flume as in the single bank tests for a given density, the width of each bank was fixed as $0.21\ m$. To enable different values of W_{Free}, the measurement area was artificially narrowed by creating temporary flume walls on the outer sides of the vegetated banks, with flow on either side, as Fig. 2b shows. Five different free flow widths were designed, with $W_{Free} = 0.7\ m$, $0.6\ m$ $0.5\ m$, $0.4\ m$ and $0.3\ m$ resulting in a total of 60 different testing conditions considering all densities and flow depths. For each experiment, the steady flow rate was measured using a volumetric measuring tank.

Rhodamine WT dye was used as a soluble tracer for all tests. A steady release of dye was injected into the flow at a single transverse location via a vertical line source uniformly drilled within its length and supplied using a constant head tank. The injector was located at $4\ m$ upstream of the measurement area to encourage vertically well-mixed conditions within the recorded area. Ten different injection positions were considered for each water depth and each vegetation density for tests with single vegetated bank condition, whilst for dual vegetated banks the dye was injected at the centreline of the free flow region (Fig. 2).

3.1 Flow measurement

To characterise the profile of streamwise velocity and evolution of depth averaged solute concentration downstream of the injection, large-scale Particle Image Velocimetry (PIV) and Planar Concentration Analysis (PCA) were implemented using synchronised GoPro cameras. The measurement system allows the rapid characterising of 2D surface velocity profiles via the imaging of PIV particles, and depth-averaged solute concentrations via the measurement of light intensity, over length scales suited to the study of mixing across interacting vegetated shear layers. Further details and validation of the measurement system can be found in Rojas-Arques et al. [34] and in Rojas-Arques [35].

Four GoPro cameras were installed above the channel and aligned with the centre of the channel width at a height of $1.2\ m$ and at intervals of $1.2\ m$, recording individual frames of $1440 \times 1920\ pixels$ with a pixel resolution of $1 \times 1\ mm$. To enable the characterisation of depth averaged solute concentrations, the measurement area was illuminated with green LED lights. A full description of the lighting setup can be found in Rojas-Arques [35].

A spatial calibration was performed to correct the fisheye distortion produced by cameras by using a standard chequerboard method. The field of view of each camera overlapped with the next, and a smoothing function was applied in this overlap region, stitching the four frames of each time step together and resulting in a combined full frame of

Table 1 Experimental conditions and resulting fitted velocity and mixing parameters for single vegetated bank tests. Reynolds number (Re) and Froude number (Fr) are calculated based on U_{Free}. y0 is measured relative to the vegetation/free-flow interface

a[1/m]	h[m]	λ[−]	$U_{Veg}\left[\frac{m}{s}\right]$	Re_{stem} [−]	$U_{Free}\left[\frac{m}{s}\right]$	Re[]−	Fr[−]	U_S [m/s]	δ_{Inner} [m]	δ_{Outer} [m]	y_0 [m]	$D_{ymax}\left[\frac{m^2}{s}\right]$
6.349	0.036	0.905	0.016	80	0.322	11592	0.54	0.052	0.066	0.389	0.008	$2.95\,10^{-4}$
6.349	0.054	0.921	0.017	85	0.412	22248	0.57	0.063	0.074	0.272	−0.007	$4.54\,10^{-4}$
6.349	0.072	0.934	0.017	85	0.500	36000	0.59	0.071	0.081	0.354	−0.002	$7.01\,10^{-4}$
6.349	0.090	0.927	0.020	100	0.529	47610	0.56	0.078	0.083	0.334	−0.003	$1.15\,10^{-3}$
1.587	0.036	0.746	0.038	190	0.261	9396	0.44	0.075	0.076	0.295	0.016	$2.24\,10^{-4}$
1.587	0.054	0.774	0.048	240	0.377	20358	0.52	0.099	0.098	0.365	0.027	$3.69\,10^{-4}$
1.587	0.072	0.791	0.051	255	0.438	31536	0.52	0.109	0.141	0.400	0.053	$6.36\,10^{-4}$
1.587	0.090	0.766	0.064	320	0.482	43380	0.51	0.129	0.136	0.346	0.023	$8.89\,10^{-4}$
0.397	0.036	0.303	0.129	645	0.241	8676	0.41	0.190	0.010	0.281	0.046	$1.51\,10^{-4}$
0.397	0.054	0.385	0.156	780	0.351	18954	0.48	0.235	0.042	0.280	0.108	$2.16\,10^{-4}$
0.397	0.072	0.404	0.166	830	0.391	28152	0.47	0.252	0.045	0.264	0.126	$3.36\,10^{-4}$
0.397	0.090	0.407	0.180	900	0.427	38430	0.45	0.273	0.061	0.316	0.098	$5.93\,10^{-4}$

$1220 \times 4480\ pixels$. A LED timer consisting of 6 columns of 10 LEDS was used to synchronise recorded frames. Before each experiment, the LED timer was recorded by each pair of cameras simultaneously over $2\,s$ and the delay time between cameras was calculated based on the images. These images could then be used for the PCA or PIV method. For the PCA (only), each $10 \times 10\,cell$ was then averaged to give concentration frames of 122×448, where each point represents an area of $10 \times 10\,mm$. Further information regarding this procedure is described in Rojas-Arques et al. [34].

Finally, a PCA calibration was performed. For each measurement cell and water depth, a polynomial function was used to fit the relationship between the measured green intensity and the known concentration [35].

3.2 PIV data analysis

The surface of the flow was seeded with $2\ mm$ black polypropylene particles with a density of $900\ kg/m^3$, obtaining a particle density of around $9\ particles/cm^2$. Individual frames obtained from the large-scale PIV technique were converted into black and white. A $10\,s$ mean background image was then obtained from each video and later subtracted from each individual frame. Instantaneous frames (80 Hz) for each test were analysed using PIV software Dynamic Studio (by Dantec Dynamics Ltd.) to obtain a time series of instantaneous longitudinal velocity matrices for each flow condition. Based on these matrix vectors, the temporal mean longitudinal velocity ($\overline{U}$) and temporal standard deviation ($\sigma_{\overline{U}}$) were obtained and all instantaneous velocity values outside the range $\overline{U} \pm 3.\sigma_{\overline{U}}$ were removed. Here $\overline{U}$ denotes the time-and space-averaged surface velocity obtained from LSPIV. It is taken to represent the depth-averaged streamwise velocity in the shallow, relatively uniform flows considered here, consistent with previous LSPIV studies demonstrating good agreement between surface and depth-averaged velocities (Mejía-Morales et al., [17]). The filtering was applied independently to the temporal velocity record at each grid cell of the velocity field, so the threshold was based on local temporal statistics rather than spatial averaging across the flow domain. The Matlab code *ndnanfilter.m* [44] which applies a multidimensional smoothing filter while ignoring NaN values, was then applied to the time-averaged longitudinal velocity maps to smooth transitions within the overlapping regions between cameras. Finally, a third-order two-dimensional median filter was applied to each time-averaged longitudinal velocity map to smooth any spikes produced during the previous processes without affecting the mean longitudinal velocity.

3.3 PCA data analysis

For each test, a time-averaged frame was obtained over $60\,s$ during the dye injection. A spatial average was applied to the green component of the RGB matrix over $10 \times 10\ pixels$ and the calibration relationship was applied. Background concentration levels (from an equivalent PCA measurement with no dye present) were removed from each 10×10 area. The remaining noise from the concentration maps was removed by applying a sixth-order two-dimensional mean filter and for each lateral transverse profile, all values smaller than $3\,\%$ of the maximum concentration value were removed to define the boundaries of the trace. This threshold was chosen because noise outside the dye plume reached between 2

and 3%. Post-filtering, a mass balance was applied to each lateral transverse profile to ensure mass conservation over the measurement length, with all such factors $< 10\,\%$.

3.4 Finite difference model

The finite difference solution to solve Eq. 3 proposed and validated by West et al., [47] was used to identify transverse mixing coefficients based on experimental data from single bank tests. To achieve this, the recorded channel was assumed as a rectangular grid with $i \times j$ nodes, with $h(y)$, $U(y)$ and $D_y(y)$ specified at each node. The equation was discretised using a central approximation for the right part of the Eq. 3 and an upwind approximation for the left part of the Eq. 3. The equation system was later solved using the Thomas algorithm approach, applying a zero-gradient lateral boundary condition $\frac{\partial C}{\partial y} = 0$ at the impermeable sidewalls (i.e. at the outer edges of the measurement domain in the transverse direction).

Similar to previous work [36, 47], a four-layer transverse diffusivity profile is used to describe the mixing process across the vegetation/free flow interface.

- In the free flow layer away from the shear layer, a constant transverse mixing coefficient within the free open flow region is defined as $D_{y_{Free}} = 0.14\,hu^*$ (where u^* is bed shear velocity defined as $u^* = \sqrt{ghS_o}$, and g is the acceleration due to gravity) based on previous experiments in the same facility [35].
- Constant transverse mixing within the vegetated bank ($D_{y_{Veg}}$) is assumed, and calculated using an expression proposed by Nepf [24] under similar experimental conditions: $D_{y_{Veg}}(Ud)^{-1} = 0.2$ for $\emptyset < 0.1$. Here $\emptyset = 0.25ad\pi$ is the solid volume fraction, which equates to between 0.0015 and 0.025 for the current study.

- Similar to previous studies (e.g. West et al., [47], a skewed Gaussian function is proposed over the inner and outer shear regions to define the profile of mixing coefficient. This formulation follows the approach proposed by Sonnenwald et al., [40] and West et al., [47], in which the transverse mixing coefficient is represented by a skewed Gaussian distribution centred at the velocity inflection point. The two variance parameters correspond to the inner and outer shear-layer thicknesses (δ_{Inner} and δ_{Outer}), reflecting the asymmetric structure of the shear layer between the vegetated and free flow regions. The width of this region is assumed to match with the shear layer region, estimated using methods to be described in Sect. 4.1, and the position of the maximum transverse mixing coefficient was considered to match with the position of the inflection point of the streamwise velocity profile (y_0). This is where the shear (velocity gradient) is maximal and turbulence production is strongest. The variance parameters that define skewed distribution in the inner (σ^2_{Inner}) and the outer layers (σ^2_{Outer}) are taken as:

$$\sigma^2_{Inner} = \frac{-\delta_{Inner}^2}{2\,ln\left(\frac{D_{y_{Veg}}}{D_{y_{max}}}\right)} \tag{4}$$

$$\sigma^2_{Outer} = \frac{-\delta_{Outer}^2}{2\,ln\left(\frac{D_{y_{Free}}}{D_{y_{max}}}\right)} \quad (5)$$

Based on these assumptions, as well as transverse profiles of streamwise velocity (Sect. 4.1) and measured flow depth, experimental solute concentration data can be used to parametrise the single variable ($D_{y_{max}}$) required to define the estimated profile of transverse mixing coefficient.

To obtain $D_{y_{max}}$ for each single vegetated bank density and flow condition, an optimisation routine was used to maximise the goodness of fit (coefficient of determination, R^2) between the simulated (Eq. 3) profiles and the experimental data over the 2D measurement area. Measured concentration profiles at the upstream edge of the measurement area are used as a boundary condition for Eq. 3. The routine equally considered data based on each of the ten injection positions (Fig. 2a), such that a single maximum mixing coefficient ($D_{y_{max}}$) was obtained for each flow condition which considered data obtained over the full shear layer [35].

The combination of LSPIV and PCA was selected for its ability to provide high-resolution, two-dimensional measurements over a wide spatial extent without disturbing the flow, offering clear advantages over intrusive point-sampling or Acoustic Doppler Velocimetry (ADV) techniques. The Finite Difference Model (FDM) was adopted for its computational efficiency and direct compatibility with the framework proposed by West et al., [47], enabling consistent comparison and extension of previous work on transverse mixing across vegetated shear layers. In the following sections, these measurement and modelling tools are combined to derive bulk parameterisations of shear-layer velocity structure (Sect. 4) and to link them to transverse mixing behaviour in single and dual-bank flows (Sect. 5).

4 Velocity profile results

Section 4 presents the velocity results and develops new parameterisations required for the analytical relationships describing mixing processes to be introduced in Sect. 5. Specifically, the section introduces (i) an empirical relationship linking vegetation projected area to the position of the velocity inflection point (y_0), and (ii) relationships expressing inner- and outer-layer shear thicknesses (δ_{inner} and δ_{outer}) in terms of vegetation density and the velocity contrast between vegetated and free flow regions. These allow the White and Nepf [49] shear-layer model to be applied using bulk vegetation and flow properties. The section then extends this approach to dual-bank configurations by proposing a parameterisation for the reduction in centreline velocity as shear layers interact. Throughout Sect. 4, regression fits use the combined datasets from the present study, White and Nepf [46, 48, 49]. West et al., [47] is also referenced for conceptual comparison.

4.1 Single vegetated bank velocity results

4.1.1 Shear-layer parameters

Mean transverse profiles of velocity were obtained from the time-averaged longitudinal velocity maps by averaging over the length of the recorded LSPIV area for each spanwise position.

Figure 3 shows the longitudinal velocity profiles from single vegetated bank flow conditions, with ranges based on standard deviation values considering all the time-averaged values along the streamwise direction. High variabilities in the mean longitudinal experimental velocity values recorded close to the right wall are likely due to a lack of PIV particles in this region during the experiments, however this does not affect measurements in the shear layer region. The fitted velocity profile model and parameterisation proposed by White and Nepf [49] is also plotted in Fig. 3 as described in Sect. 2 (Eq. 1 and 2). Here, R^2 is used only as a comparative indicator of trend agreement between methods and does not necessarily reflect absolute agreement in magnitude where systematic offsets are present.

To fit the White and Nepf [49] model for each flow condition, the mean longitudinal velocity within the vegetated bank (U_{Veg}) and within the free flow region (U_{Free}) were defined as the mean measured value inside those areas from where the velocity gradients were considered negligible (smaller than 5 % of the maximum velocity gradient). To obtain velocity within the inner and outer regions of the shear layer (U_{Inner} and U_{Outer}), Eq. 1 and 2 were fitted to the experimental data using a non-linear least-squares regression whilst varying y_m and U_m until the difference between measured and predicted velocity profiles was minimised at $y = y_m$. As a result, values of δ_{Inner}, δ_{Outer} U_S and y_o were obtained (Table 1). A high level of agreement between Eq. 1 and Eq. 2, and the observations within the shear layer region was observed (mean $R^2_{Wand\&N} = 0.996$). Velocities in Table 1 were also used to confirm the presence of large-scale Kelvin-Helmholtz vortex structures according to the velocity ratio (λ) proposed by Proust et al., [30], defined as:

$$\lambda = \frac{U_{Free} - U_{Veg}}{U_{Free} + U_{Veg}} \tag{6}$$

where $\lambda > 0.3$ indicates the potential presence of Kelvin-Helmholtz vortex structures [30, 31]. According to this criterion, in all cases, the presence of the vegetated bank induced the generation of large-scale turbulence structures.

4.1.2 New parameterisation for y_0

Based on the datasets available, Fig. 4 shows the observed relationship between deflection of the velocity inflection point (y_0) relative to the vegetation/free flow interface point and the vegetation area parameter ($a = nd$). For existing experimental data (from artificial vegetation), this shows that the position of the velocity inflection point is primarily influenced by the effective density of the vegetation, with y_0 tending to 0 for higher values ($a \approx 6\,m^{-1}$). An empirical relationship can therefore be proposed to estimate y_o based on the mean projected area per unit volume of the vegetated bank, with a correlation $R^2 = 0.834$ between the proposed relationship and the available empirical y_0 values (Fig. 4).

4.1.3 New parameterisation for δ_{inner} and δ_{outer}

A similar approach is used to determine how the inner and outer shear-layer thicknesses depend on vegetation density and velocity contrast. Figure 5 suggests a relationship between vegetation projected area (a), and relative velocity in the free flow and vegetated regions and the shear layer

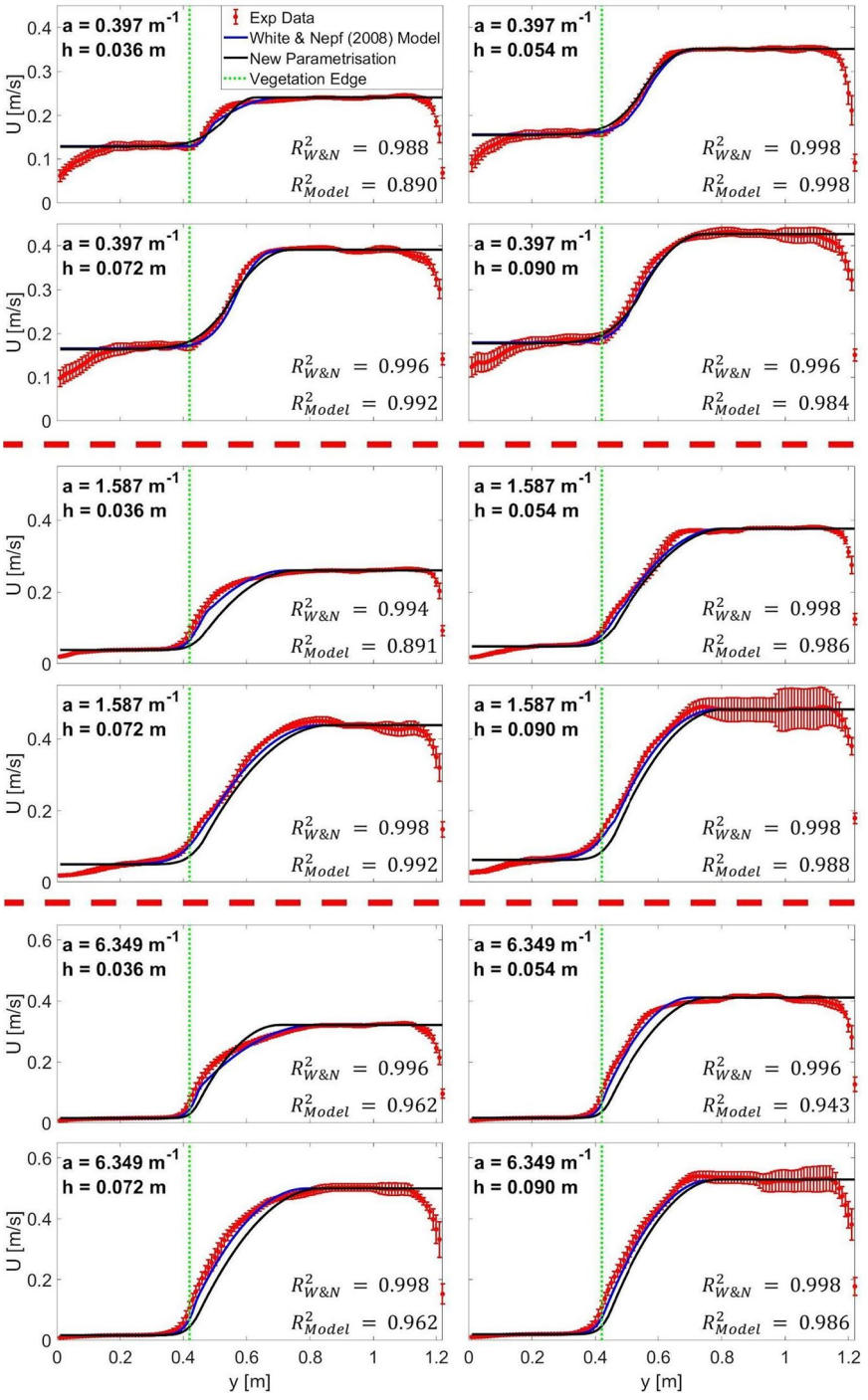


Fig. 3 Mean and standard deviation of measured profiles of streamwise velocity in single bank configurations, fitted original White and Nepf [49] model and new parameterisation. Correlation statistics based on fit within shear layer region

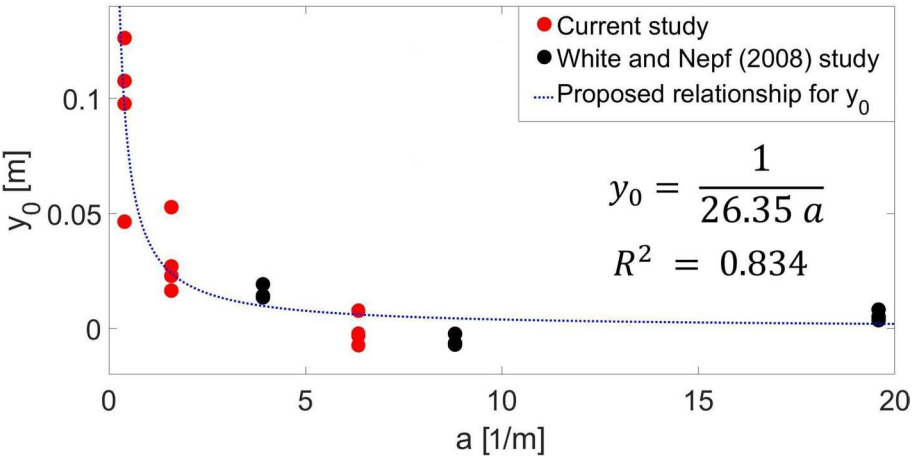


Fig. 4 Relationship between the mean projected area per unit volume of the vegetated bank ($a = nd$) and the position of inflection point relative to vegetation/free flow interface (y_0)

size, based on combined datasets from the current study and those from White and Nepf [49] and West [46] using artificial vegetation. Empirical relationships (Eq. 7 and 8) are therefore proposed to describe the size of the shear layer region based on vegetation and velocity outside the shear region. Here ΔU denotes the velocity difference between the free flow and vegetated regions.

$$\frac{\frac{\Delta U}{U_{Veg}}}{\delta_{Outer}} = 11.19\,a \tag{7}$$

$$\frac{\frac{\Delta U}{U_{Veg}}}{\delta_{Outer} + \delta_{Inner}} = 10.08\,a \tag{8}$$

4.1.4 Evaluation of the parameterised model

Based on the new parameterisations proposed in Fig. 4 and in Eq. 7 and 8, and the expressions proposed by White and Nepf [49] (Eq. 1 and 2) the profile of streamwise velocity can now be estimated based on the vegetated projected area and velocities within the vegetated bank and free flow layer.

This new parameterisation, together with mean measured values of U_{Veg} and U_{Free}, was used to estimate the lateral velocity profiles, which were then compared to experimental data (Fig. 3). The values of the coefficients of determination (R^2_{Model}) between the velocity profiles predicted by the new model parameterisation and experimental data (over the shear layer only) for each flow condition show a high agreement between predicted and experimental velocity profiles (mean $R^2_{Model} = 0.964$) although a slight decrease in the correlation is found for shallower and sparser flow conditions. Although the fit is slightly weaker than the White and Nepf [49] model, the proposed new parameterisation allows the velocity profile to be determined solely based on bulk vegetation and velocity parameters (a, U_{Veg} and U_{Free}), making it appli-

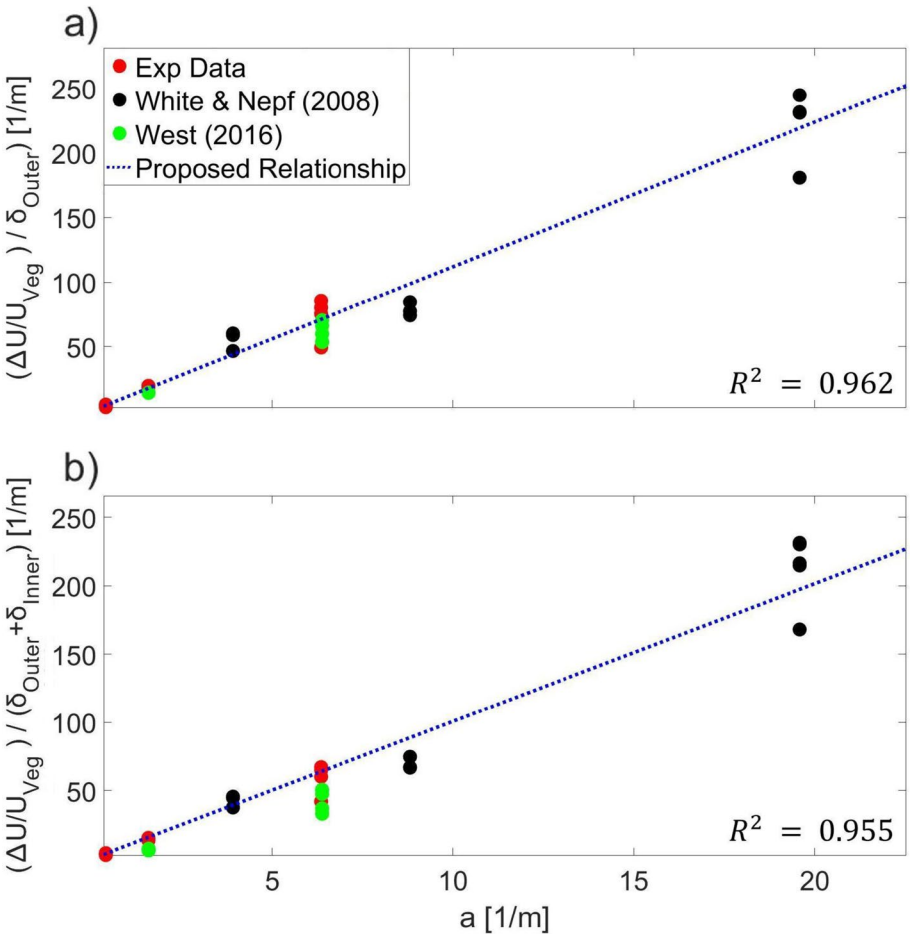


Fig. 5 Relationship between velocity increment, normalised by vegetated velocity and shear layer length, and vegetation density for: **a** outer region length; **b** total shear layer length

cable in practical situations without requiring detailed velocity measurements within the shear layer.

4.2 Dual vegetated banks velocity results

The velocity parameterisation is now extended to dual-bank configurations by introducing a simple scaling for the reduction in centreline velocity as a function of free flow width relative to shear-layer thickness, and by prescribing a parabolic form for the velocity profile between interacting shear layers.

Experimental profiles of streamwise velocity in dual bank conditions with different free flow gaps ($W_{Free} = 0.7\ m,\ 0.5\ m$ and $0.3\ m$) and water depths are plotted in Fig. 6 for all vegetation densities studied. Error bars represent the standard deviation of time averaged measurements over the lengthwise direction. The lateral position y has been normalised by the width of the central vegetation free area W_{Free}.

Figure 6 shows that as W_{Free} is reduced, the shear layers generated by the two vegetated banks start to overlap and interact, with a resulting strong gradient in streamwise velocity over the entire free flow area. The value of maximum velocity in each case occurs approximately at the channel centreline, however in cases of strong shear layer overlap, the maximum velocity is reduced when compared to the equivalent maximum velocity in free flowing conditions (U_{Free}). In the narrowest free flow configurations, particularly at higher water depths, the outer regions of the shear layers generated by each vegetated bank occupy a large proportion of the available gap width. When the outer shear-layer thickness becomes comparable to or larger than half of the free flow region, the layers cannot fully develop towards an open-channel velocity profile before interacting. The resulting overlap suppresses velocity development in the centre of the channel, producing the pronounced drop in centreline velocity visible in the upper subplots of Fig. 6.

To consider the interaction of shear layers and the associated reduction in maximum velocity the following non-dimensional relationship is proposed by the authors, based on an evaluation of the experimental data.

$$\frac{W_{Free}}{2\,\delta_{Outer}} = f\left(\frac{U_{max}}{U_{Free}}\right) \tag{9}$$

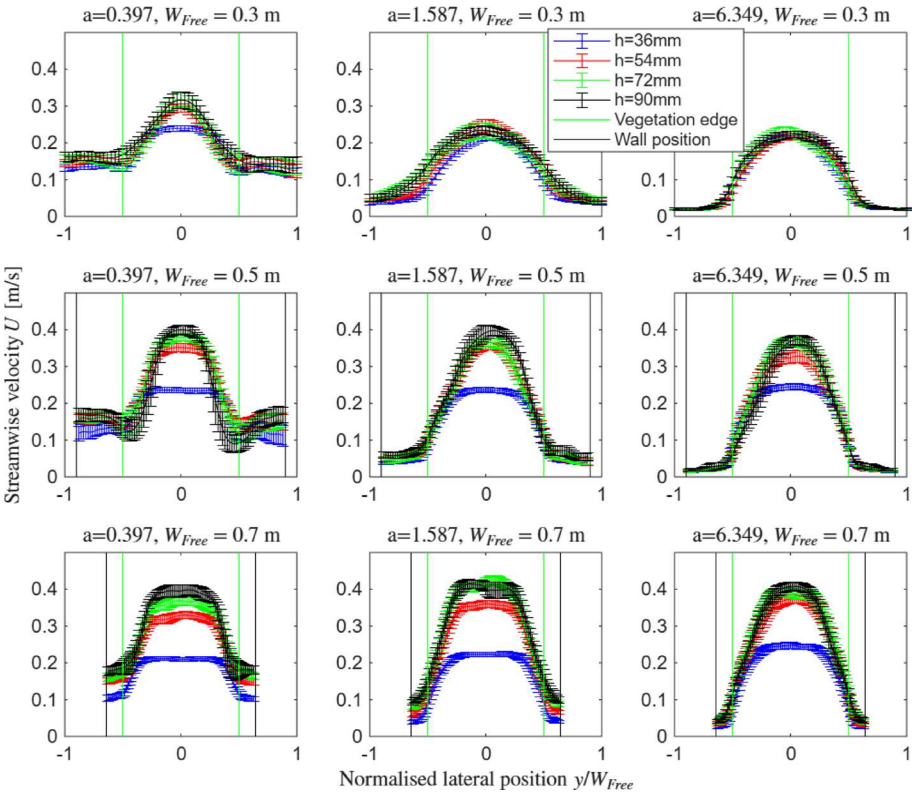


Fig. 6 Lateral profiles of mean and standard deviation of time-averaged streamwise velocity, for $W_{Free} = 0.7\,m$, $0.5\,m$ and $0.3\,m$ and each water depth for dual bank cases and all vegetation densities. The horizontal axis shows the lateral position from the flume centreline, normalised by free-flow width. Legend entries identify the flow condition by mean depth in mm, along with the lateral position of the vegetation edges and flume walls

where U_{max} is the maximum longitudinal velocity recorded at the centre of the channel and U_{Free} is the expected free flow longitudinal velocity in equivalent open channel flow without vegetation. In this case, U_{Free} was obtained from equivalent LSPIV measurements in the same channel with no vegetation, averaged over the region outside the influence of the channel sidewalls [35]. Table 2 shows the test conditions (mean projected area a and depth h), measured experimental parameters (Q, U_{Veg}, U_{Free} and U_{max}), along with δ_{Outer} values estimated from Eq. 7 for all dual bank tests.

Similar to single vegetated bank conditions, velocity ratios (λ) between free flow and vegetated velocities were calculated, suggesting the presence of large-scale coherent structures in all cases.

Experimental derived ratios within Eq. 9 are plotted for each test condition in Fig. 7. Based on the assumption of a horizontal asymptote for $\frac{W_{Free}}{2\,\delta_{Outer}} > 1$, where $U_{max} \approx U_{Free}$ (i.e., outside the shear region the maximum velocity is unchanged); an empirical function was fitted to the experimental data to define the degree of reduction in the observed maximum velocity as a function of the degree of overlap in the vegetated shear layers by considering the vegetation projected area (Eq. 10).

$$1 - \frac{U_{max}}{U_{Free}} = \frac{52.14}{100}(1 - 0.0039a)^{-52.14}\left(exp\left[\left(1 - \frac{W_{Free}}{2\delta_{Outer}}\right)^2\right] - 1\right) \tag{10}$$

This proposed relationship and observed values are plotted in Fig. 7, as well as the coefficient of determination R^2 between the proposed relationship for each vegetation density. It should be emphasised that Eq. 10 is fitted solely against the present dual-bank laboratory dataset; comparable datasets for interacting vegetated shear layers are not yet available in the literature. As such, the relationship should be applied cautiously outside the tested range of vegetation densities, flow depths, and free flow widths, and it is best viewed as a first empirical approximation rather than a universal law. The proposed relationship performs strongly in denser cases; however, the predictive power is reduced in the sparsest vegetated condition, underpredicting the reduction in centreline velocity in some cases.

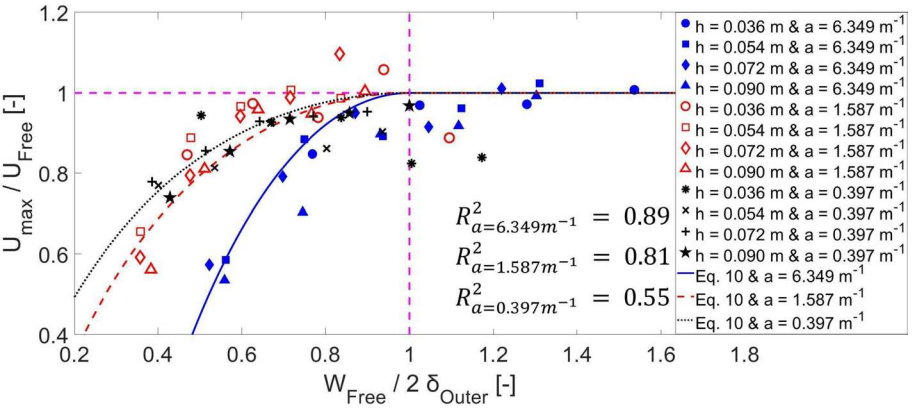


Fig. 7 Fitted relationship between free region/shear width ratio, longitudinal velocity ratio and proposed predicted relationships (Eq. 10) for all experimental cases

Given this empirical relationship to estimate U_{max} in dual bank conditions, the existing model to predict profiles of longitudinal velocity across one shear layer can be adapted to dual vegetated banks flows with overlapping shear layers. In this case a parabolic profile is assumed between velocity inflection points (y_0). This parabola has a maximum at the centre of the free flow region equal to the estimated U_{max} given by Eq. 10. The longitudinal velocity profile within the outer shear layer region (i.e. the area outside the vegetation) can be expressed as:

$$U_{Outer} = C_{1b}y^2 + C_{2b}y + C_{3b} \tag{11}$$

where:

$$C_{1b} = \frac{U(y_0) - U_{max}}{(y_0 - y_c)^2} \tag{12}$$

$$C_{2b} = -2C_{1b}y_c \tag{13}$$

$$C_{3b} = U_{max} + C_{1b}y_c^2 \tag{14}$$

where y_c is the position of the centre of the channel and y_0 is estimated using the equation obtained in Fig. 4. This proposed method was used to predict velocity profiles as shown in Fig. 8 and compared against experimental data for water depth $h = 0.054\,m$ and a mean projected area $a = 6.349\,m^{-1}$ over different W_{Free} values. In this case, U_{Veg} was obtained averaging experimental values for the different W_{Free} obtained in Table 2 for each water depth and vegetation density. More comparisons between predicted and experimental velocity profiles for other flow conditions can be found at Rojas-Arques [35].

Coefficients of determination (R^2) were calculated to compare the mean measured and predicted velocity profiles over the full width for each projected area a and W_{Free}. Results show a mean $R^2$of 0.92, 0.96 and 0.98 for $a = 0.397\,m^{-1}$, $1.587\,m^{-1}$ and $6.349\,m^{-1}$ respectively (averaged over all water depths).

The predicted profiles plotted in Fig. 8 and R^2 values obtained for each flow condition suggest a generally good fit to the experimental velocity profiles, with some deviations due to differences in predicted and observed U_{Veg} values. Results for $a = 6.349\,m^{-1}$ show a strong agreement between the prediction and experimental data, whilst the largest differences were found for the lowest a values, in which most of the experimental data exhibit a constant free flow velocity region ($U_{max} \approx U_{Free}$) in the centre of the channel, even for relatively small $\frac{W_{Free}}{2\,\delta_{Outer}}$ ratios. This is likely due to the reduced predictive performance of Eq. 10 in sparsely vegetated conditions.

It should be noted that the model is designed to capture the dominant features of the shear layers and free flow region rather than detailed flow variations within the vegetated banks. In the widest free flow case (W_{Free}= 0.7 m), measured velocities inside the vegetation show increased spatial variability and measurement uncertainty due to stem-scale wakes and wall effects, leading to larger local deviations from the simplified prediction. Nevertheless, the model reproduces the overall shear-layer position and outer-region velocities well.

Table 2 Experimental parameters for each flow condition for dual vegetated bank tests. Reynolds number (Re) and Froude number (Fr) are calculated based on U_{Free}

a [1/m]	W_{Free} [m]	h [m]	λ [−]	$U_{Veg}\left[\frac{m}{s}\right]$	Re_{stem} [−]	$U_{Free}\left[\frac{m}{s}\right]$	$U_{max}\left[\frac{m}{s}\right]$	Re [−]	Fr [−]	δ_{Outer} [m]
6.349	0.7	0.036	0.882	0.015	76.99	0.251	0.246	8870.51	0.41	0.195
6.349	0.6	0.036	0.891	0.015	72.90	0.251	0.253	9121.57	0.43	0.195
6.349	0.5	0.036	0.876	0.016	81.09	0.251	0.244	8797.12	0.41	0.195
6.349	0.4	0.036	0.858	0.019	93.47	0.251	0.244	8774.58	0.41	0.195
6.349	0.3	0.036	0.831	0.02	98.33	0.251	0.213	7679.97	0.36	0.195
6.349	0.7	0.054	0.913	0.017	84.59	0.364	0.373	20139.95	0.51	0.267
6.349	0.6	0.054	0.910	0.016	82.27	0.364	0.35	18924.16	0.48	0.267
6.349	0.5	0.054	0.898	0.017	86.91	0.364	0.325	17552.15	0.45	0.267
6.349	0.4	0.054	0.879	0.021	103.43	0.364	0.322	17407.52	0.44	0.267
6.349	0.3	0.054	0.830	0.02	98.91	0.364	0.213	11518.21	0.29	0.267
6.349	0.7	0.072	0.917	0.017	84.00	0.386	0.39	28057.64	0.46	0.287
6.349	0.6	0.072	0.911	0.016	82.18	0.386	0.353	25400.96	0.42	0.287
6.349	0.5	0.072	0.910	0.017	85.82	0.386	0.366	26380.05	0.44	0.287
6.349	0.4	0.072	0.878	0.02	99.47	0.386	0.305	21979.73	0.36	0.287
6.349	0.3	0.072	0.835	0.02	99.22	0.386	0.221	15920.28	0.26	0.287
6.349	0.7	0.09	0.907	0.02	99.27	0.410	0.407	36607.07	0.43	0.269
6.349	0.6	0.09	0.910	0.018	88.65	0.410	0.376	33864.99	0.40	0.269
6.349	0.5	0.09	0.887	0.022	109.89	0.410	0.368	33103.80	0.39	0.269
6.349	0.4	0.09	0.860	0.022	108.25	0.410	0.288	25932.31	0.31	0.269
6.349	0.3	0.09	0.827	0.021	104.11	0.410	0.219	19730.93	0.23	0.269
1.587	0.7	0.036	0.718	0.037	183.66	0.251	0.223	8043.30	0.38	0.320
1.587	0.6	0.036	0.764	0.036	177.79	0.251	0.266	9574.67	0.45	0.320
1.587	0.5	0.036	0.723	0.038	189.54	0.251	0.236	8499.90	0.40	0.320
1.587	0.4	0.036	0.713	0.041	205.04	0.251	0.245	8814.02	0.41	0.320
1.587	0.3	0.036	0.710	0.036	180.85	0.251	0.213	7663.17	0.36	0.320
1.587	0.7	0.054	0.785	0.043	216.02	0.364	0.36	19412.38	0.49	0.419
1.587	0.6	0.054	0.797	0.042	207.56	0.364	0.367	19804.51	0.50	0.419
1.587	0.5	0.054	0.774	0.045	224.49	0.364	0.352	19016.25	0.48	0.419

Table 2 (continued)

a [1/m]	W_{Free} [m]	h [m]	λ [−]	$U_{Veg}\left[\frac{m}{s}\right]$	Re_{stem} [−]	$U_{Free}\left[\frac{m}{s}\right]$	$U_{max}\left[\frac{m}{s}\right]$	Re [−]	Fr [−]	δ_{Outer} [m]
1.587	0.4	0.054	0.756	0.045	225.36	0.364	0.324	17488.83	0.44	0.419
1.587	0.3	0.054	0.705	0.041	206.35	0.364	0.239	12904.73	0.33	0.419
1.587	0.7	0.072	0.797	0.048	239.40	0.386	0.423	30449.74	0.50	0.420
1.587	0.6	0.072	0.793	0.044	219.65	0.386	0.381	27452.87	0.45	0.420
1.587	0.5	0.072	0.772	0.047	233.57	0.386	0.363	26156.40	0.43	0.420
1.587	0.4	0.072	0.749	0.044	219.47	0.386	0.306	22055.29	0.36	0.420
1.587	0.3	0.072	0.668	0.045	226.52	0.386	0.228	16417.67	0.27	0.420
1.587	0.7	0.09	0.792	0.048	239.23	0.410	0.411	37022.94	0.44	0.391
1.587	0.6	0.09	0.753	0.055	274.24	0.410	0.389	34965.02	0.41	0.391
1.587	0.5	0.09	0.740	0.059	292.91	0.410	0.393	35360.23	0.42	0.391
1.587	0.4	0.09	0.762	0.045	224.11	0.410	0.332	29903.64	0.35	0.391
1.587	0.3	0.09	0.633	0.052	258.51	0.410	0.23	20699.52	0.24	0.391
0.397	0.7	0.036	0.389	0.093	465.04	0.251	0.211	7604.51	0.36	0.298
0.397	0.6	0.036	0.343	0.102	507.76	0.251	0.206	7469.26	0.35	0.298
0.397	0.5	0.036	0.364	0.11	550.47	0.251	0.236	8500.32	0.40	0.298
0.397	0.4	0.036	0.347	0.113	565.35	0.251	0.233	8397.69	0.39	0.298
0.397	0.3	0.036	0.317	0.123	615.01	0.251	0.237	8546.24	0.40	0.298
0.397	0.7	0.054	0.422	0.134	669.18	0.364	0.329	17771.99	0.45	0.374
0.397	0.6	0.054	0.382	0.141	702.82	0.364	0.314	16956.73	0.43	0.374
0.397	0.5	0.054	0.392	0.147	736.47	0.364	0.337	18191.12	0.46	0.374
0.397	0.4	0.054	0.398	0.128	637.88	0.364	0.297	16013.65	0.41	0.374
0.397	0.3	0.054	0.348	0.136	677.58	0.364	0.28	15137.90	0.39	0.374
0.397	0.7	0.072	0.432	0.146	728.47	0.386	0.368	26467.41	0.44	0.389
0.397	0.6	0.072	0.448	0.138	691.64	0.386	0.363	26155.28	0.43	0.389
0.397	0.5	0.072	0.465	0.131	654.82	0.386	0.358	25807.46	0.43	0.389
0.397	0.4	0.072	0.387	0.146	730.18	0.386	0.33	23764.62	0.39	0.389
0.397	0.3	0.072	0.347	0.146	727.99	0.386	0.3	21607.01	0.36	0.389
0.397	0.7	0.09	0.417	0.163	815.39	0.410	0.397	35702.80	0.42	0.350

Table 2 (continued)

a [1/m]	W_{Free} [m]	h [m]	λ [−]	$U_{Veg}\left[\frac{m}{s}\right]$	Re_{stem} [−]	$U_{Free}\left[\frac{m}{s}\right]$	$U_{max}\left[\frac{m}{s}\right]$	Re [−]	Fr [−]	δ_{Outer} [m]
0.397	0.6	0.09	0.408	0.164	817.97	0.410	0.389	35034.29	0.41	0.350
0.397	0.5	0.09	0.400	0.164	820.55	0.410	0.383	34486.81	0.41	0.350
0.397	0.4	0.09	0.377	0.158	792.13	0.410	0.35	31528.52	0.37	0.350
0.397	0.3	0.09	0.329	0.153	764.16	0.410	0.303	27261.17	0.32	0.350

5 Transverse mixing results

This section first utilises experimental data to relate the $D_{y_{max}}$ parameter to the product of water depth and the velocity difference between vegetated and free flow regions, $h(U_{Free} - U_{Veg})$. This parameterisation and the associated mixing-profile assumptions described in Sect. 3.4 are evaluated against measured concentration fields for single-bank as well as dual-bank configurations with interacting shear layers.

5.1 Parameterisation of the profile of transverse mixing coefficient

Calculated concentration distributions for each single bank case were derived based on the assumed profile of transverse mixing coefficient fitted to the experimental data (as described in Sect. 3.4 based on measured water depth and profiles of streamwise velocity obtained using the proposed velocity model parameterisation described in Sect. 4.1). Resulting $D_{y_{max}}$ values for each condition are shown in Table 1. A strong non-dimensional relationship ($R^2 = 0.962$) was found between the value of $D_{y_{max}}$ and the product of the velocity difference ($U_{Free} - U_{Veg}$) and the water depth (h) over all single bank tests considered (Fig. 9). Based on these results, a new relationship (Fig. 9) is proposed.

5.2 Single vegetated bank results

The empirical relationship for $D_{y_{max}}$ proposed in Fig. 9, the assumptions considered in Sect. 3.4 and the predicted longitudinal velocity profile obtained by the analytical model explained in Sect. 4.1 were applied to predict the concentration maps using Eq. 3. Results are compared against experimental data for each injection position. Figure 10a shows the comparison between the predicted and experimental transverse concentration profile for two longitudinal positions located at $x = 1.5\,m$ and $x = 3\,m$ respectively for a mean projected area of $a = 6.349\,m^{-1}$, a water depth of $h = 0.072\,m$ and an injection located at $x = 0.52\,m$. More visual comparisons between experimental and predicted concentration profiles for different densities, water depth and injection points can be found in Rojas-Arques [35]. In addition, Fig. 10b shows the relative differences in concentration between the predicted and the experimental concentration maps for each cell based on the maximum concentration value recorded for the entire concentration map, where positive values mean an over-prediction of the concentration values and negative values mean an under-prediction of the concentration values.

Comparison between experimental and predicted data plotted in Fig. 10 suggests a good prediction of the overall concentration distribution using the proposed predictive model. Table 3 presents the mean coefficient of determination (R^2) between experimental and predicted concentrations over the 2D measurement area, with statistics calculated based on results from all the different injection conditions tested (see Fig. 2). In addition, the mean, maximum and minimum relative decreases of the experimental peak concentration over the measurement area (PR) are shown.

Differences between experimental and predicted data shown in Fig. 10 suggest a displacement of the solute mass towards the vegetation boundary relative to the model predictions. More displacement was observed for experimental data with the densest vegetation and the highest flow depths. This movement may be produced by secondary currents gener-

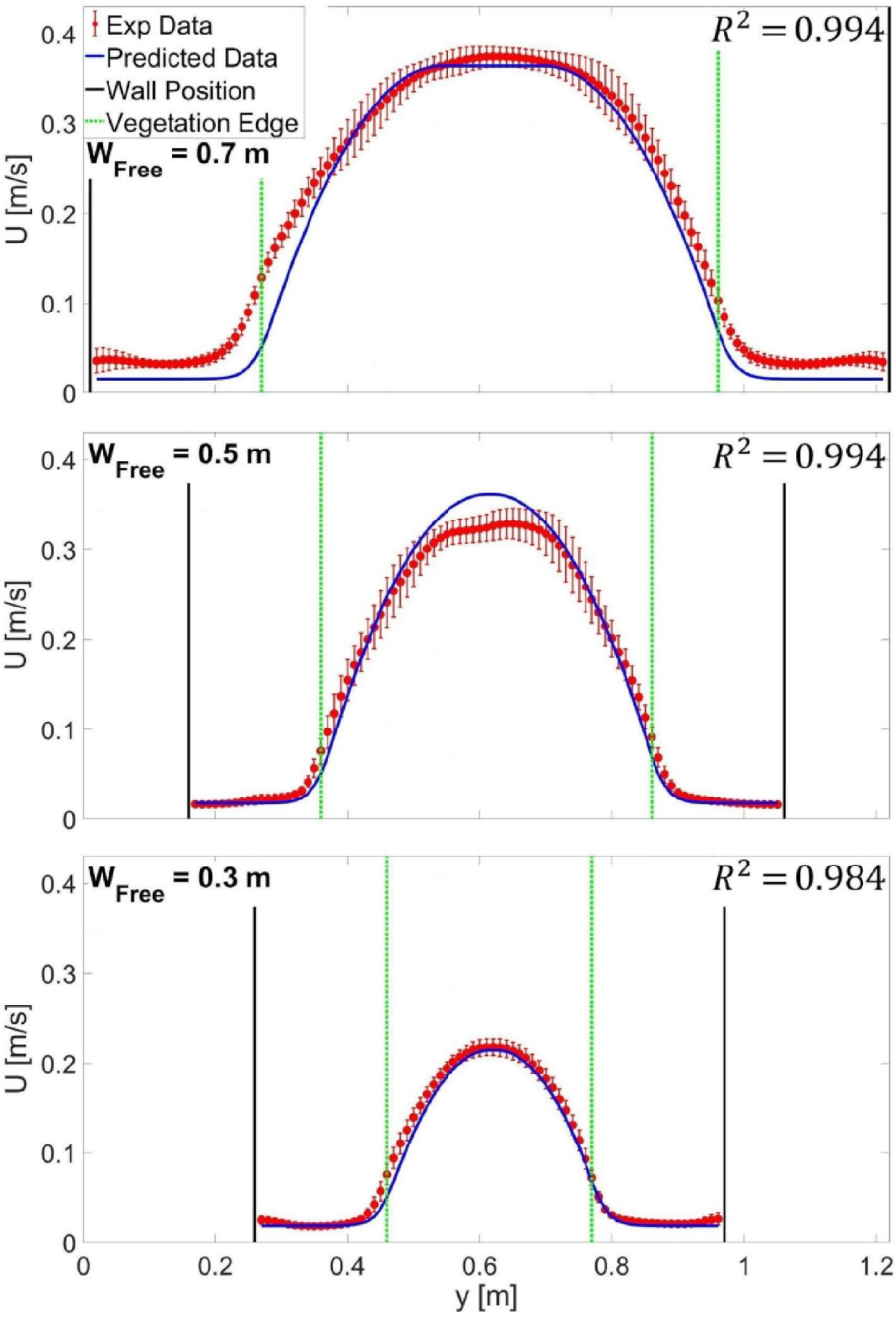


Fig. 8 Experimental and predicted time-averaged mean longitudinal velocity profiles for dual vegetated banks flow condition for a water depth of 0.054 m and a vegetation density of $a = 6.349m^{-1}$. Correlation statistics based on fit over the full width

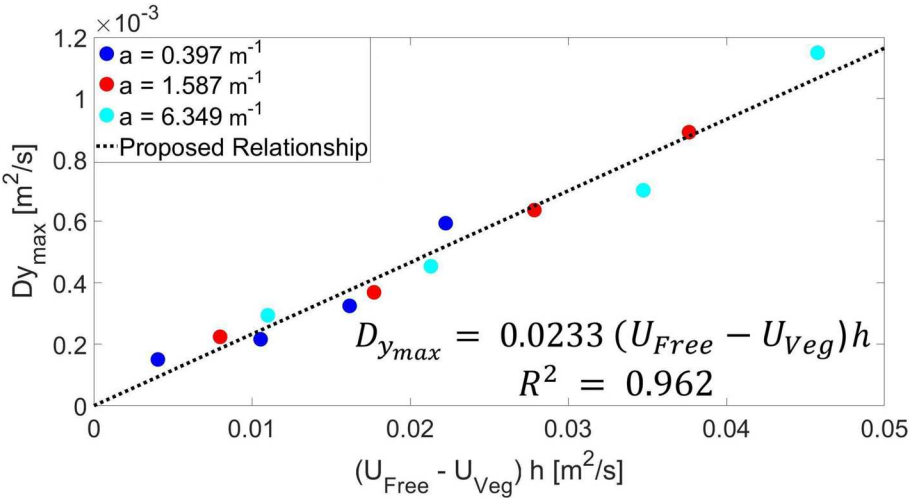


Fig. 9 Relationship between maximum transverse mixing coefficient ($D_{y_{max}}$) and the product of velocity difference ($U_{Free} - U_{Veg}$) and water depth (h) in single bank tests

ated along the water depth close to the vegetation boundary, which seem to be dependent on the velocity difference ($U_{Free} - U_{Veg}$) and the water depth. These three-dimensional motions are not explicitly represented in the present depth-averaged modelling framework and therefore may contribute to the remaining discrepancies between predicted and measured concentration fields. Moreover, experimental peak reductions (PR) shown in Table 3 suggest an increase of mixing (i.e., larger reduction in peak concentration) with vegetation projected area (as may be expected from the relationship shown in Fig. 9).

5.3 Dual vegetated banks concentration results

Based on a similar procedure to the above, Fig. 11a, c and e, presents example comparisons between experimental and predicted concentration profiles for different free flow widths ($W_{Free} = 0.7\,m,\ 0.6\,m$ and $0.5\,m$ respectively) shown for $h = 0.072\,m$ and $a = 6.349\,m^{-1}$. In addition, relative differences between both predicted and experimental concentration maps divided by the maximum concentration value were plotted in Fig. 11b, d and f.

Relative differences between predicted and measured values are plotted in Fig. 11b, d and f, where positive values mean an over-estimation of concentration values and negative values mean an under-estimation of concentration values. Similarly, to single bank tests, experimental results suggest a displacement of concentration mass toward the vegetation boundaries relative to the predictions.

Note that the transects shown in Fig. 11 represent cross-channel concentration profiles extracted at a single downstream position for each configuration. The mean R^2 values reported in Table 4, by contrast, quantify the overall agreement between measured and predicted concentration fields across the full measurement domain. Local deviations visible in the transects, particularly for the widest free flow cases, reflect spatial variations and secondary flow effects not captured by the one-dimensional framework.

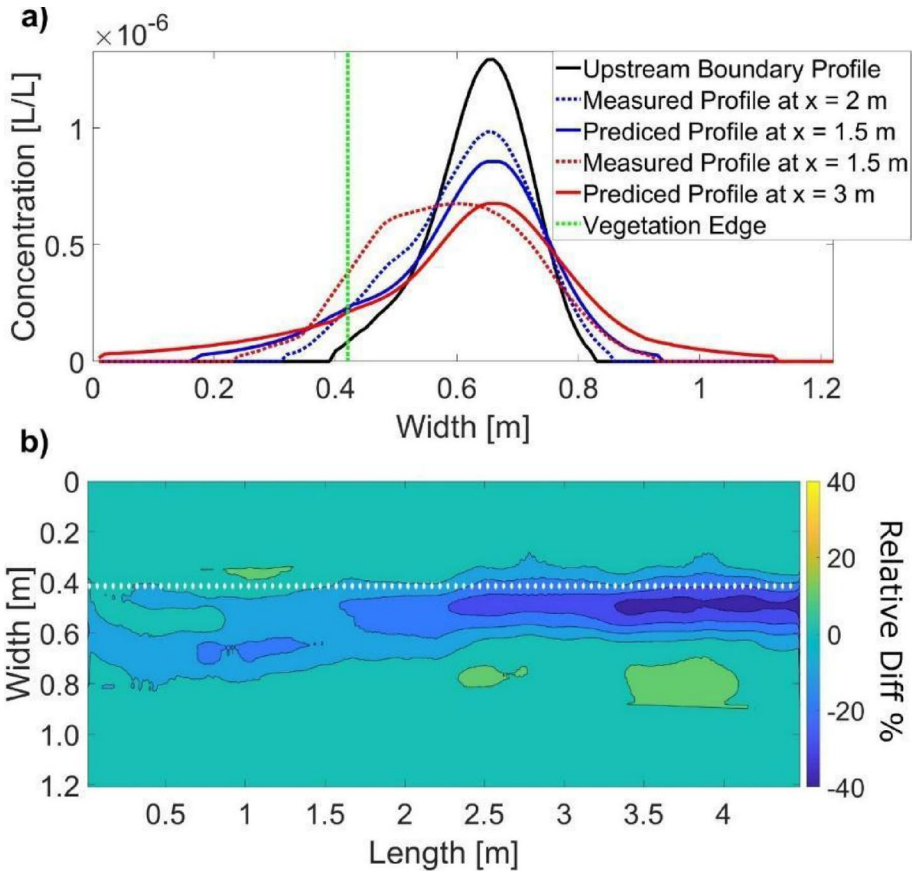


Fig. 10 Comparison between time-averaged predicted and experimental concentration data for a $h = 0.072\,m$, $a = 6.349\,m^{-1}$ and injection at $x = 0.52\,m$ for **a** transverse profiles located at $x = 1.5\,m$ and $x = 3\,m$ and **b** relative differences between predicted and experimental concentration values

The values of the coefficients of determination R^2 between modelled and experimental concentration maps were calculated for each flow condition over the measurement area. Table 4 shows the mean, max and min R^2 obtained over each vegetation density and W_{Free} flow condition (i.e., statistics are calculated based on results for the range of flow depths). The calculated R^2 values suggest a generally good prediction of mixing processes for each flow condition. The highest differences were observed for the densest scenarios and $W_{Free} = 0.7\,m$ and $0.6\,m$. In addition, the mean, maximum and minimum relative reduction of the experimental peak concentration (PR) over the measurement area is shown. For $a = 0.397\,m^{-1}$, observed peak reductions in concentration tend to increase as the W_{Free} is reduced, whilst the opposite trend is observed for $a = 6.349\,m^{-1}$. The results also demonstrate a significant increase in overall mixing/ peak concentration reduction compared to single vegetated bank scenarios with equivalent projected areas. Full results and comparisons between experimental and predicted concentration profiles can be found in Rojas-Arques [35].

Table 3 Mean, max and min coefficients of determination (R^2) between predicted and experimental concentration maps across dye injection positions, and reduction in experimental peak concentration over the measurement length for single bank tests

a[1/m]	h[m]	Mean R^2	Max R^2	Min R^2	Mean PR[%]	Max PR[%]	Min PR[%]
0.397	0.036	0.98	0.98	0.96	25.44	29.23	20.93
0.397	0.054	0.98	0.98	0.98	42.90	49.53	35.34
0.397	0.072	0.96	0.98	0.96	37.73	44.81	30.40
0.397	0.09	0.92	0.94	0.90	32.46	38.77	28.59
1.587	0.036	0.96	0.98	0.92	34.69	48.25	19.08
1.587	0.054	0.96	0.98	0.94	45.36	54.80	35.72
1.587	0.072	0.98	0.98	0.96	44.36	49.79	40.53
1.587	0.09	0.96	0.98	0.94	44.35	51.23	36.73
6.349	0.036	0.94	0.96	0.92	43.10	50.44	30.68
6.349	0.054	0.94	0.96	0.90	49.75	57.47	41.10
6.349	0.072	0.94	0.98	0.90	48.91	53.13	41.79
6.349	0.09	0.92	0.96	0.88	44.52	51.87	38.08

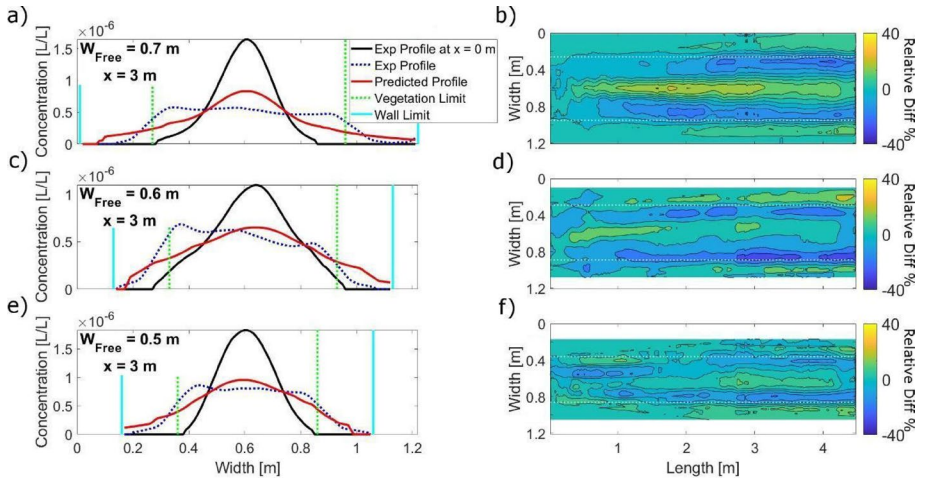


Fig. 11 Time-averaged concentration results for $h = 0.072\,m$ and $a = 6.349\,m^{-1}$ for (**a-c-e**) experimental and predicted profile comparison at $x = 3\,m$, and (**b-d-f**) differences between experimental and predicted maps divided by the maximum concentration at each transverse profile

The reduced agreement for dense vegetation and large free flow widths (Table 4) may reflect processes not represented in the simplified one-dimensional transverse mixing framework used here. Previous studies have shown that shear-layer dynamics and secondary motions can influence transverse momentum and scalar transport in vegetated or compound-channel flows (e.g. Dupuis et al. [6, 7]). Such mechanisms may contribute to the observed displacement of the concentration plume towards the banks, even though the underlying velocity profiles remain well reproduced.

Table 4 Mean, max and min coefficients of determination (R^2) between predicted and experimental concentration maps over each depth condition for each vegetation density and free flow width, and percentage of peak reduction over the measurement area

a[1/m]	W_{Free} [m]	Mean R^2	Max R^2	Min R^2	Mean PR[%]	Max PR[%]	Min PR[%]
0.397	0.7	0.96	0.98	0.92	54.45	58.83	49.77
0.397	0.6	0.96	0.98	0.94	45.89	49.02	43.10
0.397	0.5	0.96	0.98	0.94	36.92	44.93	30.55
0.397	0.4	0.98	0.98	0.96	41.74	51.19	34.02
0.397	0.3	0.98	0.98	0.98	34.06	43.36	24.33
1.587	0.7	0.96	0.98	0.96	59.44	64.86	52.85
1.587	0.6	0.98	0.98	0.96	65.13	69.32	61.54
1.587	0.5	0.98	0.98	0.98	61.25	67.41	55.73
1.587	0.4	0.98	0.98	0.96	62.04	72.64	52.43
1.587	0.3	0.94	0.98	0.94	56.00	66.08	32.64
6.349	0.7	0.88	0.94	0.85	51.45	55.86	48.38
6.349	0.6	0.88	0.92	0.87	52.65	61.79	49.30
6.349	0.5	0.96	0.98	0.94	62.35	63.61	60.42
6.349	0.4	0.96	0.98	0.94	58.22	63.36	54.09
6.349	0.3	0.98	0.98	0.96	67.25	71.35	63.32

6 Discussion

6.1 Velocity profiles

Observed flow structures in single bank systems are in general agreement with previous findings [48, 49]. This includes movement of the velocity profile inflection point away from the vegetation boundary for lower projected areas of bank vegetation ($a < 6\ m^{-1}$), and increasing shear layer size as the relative difference between the mean velocity in the vegetated and free flow regions increases. This is despite differences in measurement techniques used in the studies (LSPIV vs. ADV) and the use of surface rather than depth averaged velocities. By combining datasets from the present study with those from White and Nepf [48, 49] and West et al. [46], a new parameterisation based on measurable bulk vegetation and channel properties is presented. This allows full transverse profiles of streamwise velocity in similar rigid arrays to be obtained based either on direct measurements of U_{Veg} and U_{Free} or using existing relationships (e.g. Jordanova et al., [14] to define flow conditions in the vegetation layer, and channel properties (such as slope and roughness) to estimate free flow velocity and hence relative velocity difference ($U_{Free} - U_{Veg}$). It should however be noted that such parameterisations assume rigid emergent vegetation with drag characteristics that can be represented using established bulk drag formulations. In contrast, natural vegetation often exhibits flexibility and flow-induced reconfiguration, which modifies the effective drag coefficient as a function of flow velocity and vegetation morphology. Caroppi et al., [3] demonstrated that vegetation structure and reconfiguration influence coherent shear-layer dynamics and momentum exchange at the vegetation-free flow interface. In such cases, the drag coefficient cannot be treated as constant, so incorporating flow-dependent drag formulations would likely improve the predictive performance in field applications. The analytical framework proposed here is compatible with such extensions, provided that appropriate relationships for effective vegetation drag are specified.

In dual bank systems featuring interacting shear layers, strong gradients in streamwise velocity over the transverse profile and a reduction in the maximum channel velocity (relative to a freely flowing channel) are observed. A new empirical relationship is proposed to relate the degree of overlap of the shear layers and the reduction of the maximum streamwise velocity expected in the free flow region (relative to a fully unobstructed channel), with a decrease of maximum streamwise velocity for narrower free flow regions and denser vegetation. A new parabolic relationship is used to describe transverse profiles of streamwise velocity in these systems, with the resulting estimated profiles showing a generally good agreement with experimental data. The largest differences between predicted and recorded longitudinal velocity profiles were found for the sparsest vegetated density cases. Complementary large-eddy simulation and particle-based modelling studies of shallow free-surface flows over rough beds have similarly demonstrated that bed-generated coherent structures strongly influence free-surface dynamics and turbulence statistics ([9, 50]), underscoring the wider relevance of capturing coherent motions when interpreting shear-layer interactions at the free-surface of partially vegetated channels. For a more detailed understanding, further work considering how the interaction of shear layers affects the formation or large-scale coherent flow structures, and their effect on the streamwise velocity profile, would be of value.

It should be noted that the velocities in the vegetation and the main channel are required model inputs. In practical applications, the representative velocities in the main channel and vegetated regions can be estimated using established open-channel flow relations and vegetation resistance formulations, rather than requiring direct velocity measurements.

6.2 Transverse mixing

The work in this paper extends the framework proposed by West et al., [47] for mixing in partially vegetated channels, which emphasises heterogeneity in transverse diffusion coefficients across shear layers. The empirical relationships presented here provide a complementary predictive tool that incorporates vegetation and flow parameters into a simplified form compatible with their model. The new equations offer a directly usable parametric relationship for $D_{y_{max}}$ from which the profile of transverse mixing coefficient over the shear layer can be derived, suitable for predictive modelling applications. This assumes that mixing rates and velocities in the free flow and vegetated regions can be reasonably well described by established relationships and that mixing rates in free and vegetated flow regions are significantly lower than within the shear layer itself.

Based on the datasets collected here, this approach gives reasonably good representation of solute evolution in single bank tests. However, model results for some test conditions show a mismatch with observed data. This mismatch is represented by a movement of the observed main body of the tracer concentration toward the vegetated bank, which the proposed model does not predict. This movement would be produced by secondary currents as was discussed in Dupuis et al., [6, 7]. Similar free-surface manifestations of coherent turbulence structures have been reported in shallow flows without vegetation [22], reinforcing the central role of shear-layer dynamics in shaping the transverse mixing behaviour observed here. Such secondary motions generate lateral momentum exchange and cross-channel circulation that can advect tracer mass towards the vegetation boundary, producing deviations from the transverse diffusion assumption adopted in the present model. However, this effect

was only observed for test conditions with the highest vegetation density ($a = 6.349\ m^{-1}$) and water depth ($h = 0.072\ m$ and $h = 0.090\ m$).

This approach has also been applied to dual bank systems with interacting shear layers, accounting for the expected reduction in the maximum velocity as previously described. Both modelled results and experimental data show an overall increase in mixing rate over the channel width relative to single bank cases for the equivalent volume of vegetation, showing the potential of dual vegetated bank systems to rapidly disperse pollutants. This increase is due to the two shear layers generated for these new flow conditions increasing the overall region affected by the enhanced turbulence and thus mixing. However, relative peak reductions obtained for narrower free flow regions ($U_{Free} = 0.3\ m$) suggest a decrease of the overall mixing rate compared with other dual bank scenarios because of the restricted free velocity region allowed between both vegetated banks (this decreasing the magnitude of the overall channel velocity shear effects), which is also coupled with an increase of the overall drag and thus a reduction of the channel capacity. The effectiveness of dual bank systems in reducing peak concentration is therefore also a function of the velocity difference between free and vegetated regions, with larger shear layer overlaps resulting in reduced peak and differential ($U_{Free} - U_{Veg}$) velocities.

Comparison between predicted and experimental concentration profiles in dual bank configurations show an over-estimation of concentration values in the centre of the free flow region for the densest and deepest flow conditions, while an under-estimation is produced close to the vegetation edge. This effect is more relevant for wider free flow regions ($U_{Free} = 0.7 - 0.6\ m$). Similarly to the single bank tests this mismatch is linked with the lateral displacement of the main concentration body towards the vegetated banks. Observations of lateral displacement of tracer mass into the vegetated bank region suggest that the enhanced shear layer may promote pollutant entrainment into vegetation, increasing potential treatment or retention, whereas wider free flow regions may delay lateral entrainment and thus extend plume residence in the main channel. These findings thus point to the value of embedding vegetation-induced shear-layer dynamics into predictive models for pollutant dispersion and retention in vegetated waterways.

6.3 Limitations and opportunities for future work

Further investigations are required to study how the proposed models work in different vegetation types including flexible and natural stems, including the effects of complex turbulent structures and more significant variations in drag [3]. The present study is limited to emergent rigid vegetation; extending the proposed relationships to flexible and natural vegetation represents an important topic for future work.

7 Conclusions

This paper presents a novel set of experimental data for different scenarios with emergent rigid vegetated bank flows in single and dual configurations, obtaining the time-averaged longitudinal velocity and the concentration distribution downstream of steady state injections. Measurement techniques used in this paper allow a relatively large number of experimental conditions to be tested, which includes numerous transverse injection positions to

define mixing over the full shear layer. From this extensive experimental dataset together with results from previous work, empirical relationships were proposed to relate different parameters with the bulk vegetation characteristic data. As a result, an empirically parametrised modelling framework was developed to predict the longitudinal velocity profile and the variable transverse mixing coefficient in vegetated bank flows.

Experimental data revealed that the overlapping of the shear layers produced a decrease of the maximum longitudinal velocity achieved in the centre of the free flow region and an increase in overall transverse mixing when the shear layer produced by each vegetated bank overlaps. For an equivalent volume of vegetation, overall mixing is increased in dual bank systems compared to single bank arrangements, due to the increased size of the total shear layer region. However different and complex behaviours are observed, with density, flow depth and degree of shear overlap resulting in different velocity differential between vegetated and free flow regions affecting the shear layer characteristics and resultant mixing coefficients.

The proposed model was employed to predict the streamwise velocity profile and the mixing rate in dual vegetated bank flows, demonstrating a good agreement with experimental data in most cases, however further datasets are required to improve the model for sparsely vegetated conditions. The new relationships require fewer parameters/input data than existing models to define velocity profiles and mixing processes in flows with vegetated banks. Predictions are possible based solely on vegetated characteristics, bulk flow rate and water depths (which can be estimated based on existing relationships) in the absence of more detailed datasets. As such the relationships proposed here may form a useful tool for the initial estimation of the effects of vegetated banks on hydrodynamic and pollutant transport processes. However, further testing is required in more realistic vegetation and at field scale, including experiments with flexible and real vegetation.

The new parameterisations developed in this study provide a practical means of estimating velocity and mixing characteristics in partially vegetated channels using only bulk flow and vegetation properties. These relationships can be directly incorporated into analytical or numerical models to represent sub-grid scale mixing in larger-scale river or floodplain simulations. In field applications, they could support the preliminary assessment of pollutant dispersion or habitat connectivity in channels with vegetated margins, without the need for detailed local velocity measurements.

Acknowledgements Experimental work within this paper was funded by Engineering and Physical Sciences Research Council (EPSRC) through Grant EP/K01952X/1.

Author contributions A.N. and J.S. conceived the project. S.R-A. conducted all laboratory experiments and primary data analysis under the supervision of A.N. and J.S. J.S. led the transverse-mixing methodology and interpretation, while A.N. led the sensing and measurement approach, and novel experimental techniques. S.R-A. prepared the initial manuscript draft with oversight and editing from A.N. and J.S. A.N. led the revisions and restructuring for the resubmitted manuscript. All authors reviewed and approved the final version.

Data availability All data is available by contacting the corresponding author.

Declarations

Conflict of interest The authors declare no conflict of interest.

Open Access This article is licensed under a Creative Commons Attribution 4.0 International License,

which permits use, sharing, adaptation, distribution and reproduction in any medium or format, as long as you give appropriate credit to the original author(s) and the source, provide a link to the Creative Commons licence, and indicate if changes were made. The images or other third party material in this article are included in the article's Creative Commons licence, unless indicated otherwise in a credit line to the material. If material is not included in the article's Creative Commons licence and your intended use is not permitted by statutory regulation or exceeds the permitted use, you will need to obtain permission directly from the copyright holder. To view a copy of this licence, visit http://creativecommons.org/licenses/by/4.0/.

References

1. Bejestan MS, Yabbarehpour E, Kashefipour SM (2021) Enhancing transverse mixing by using triangular vane in the straight channel. Ain Shams Eng J 12(2):1385–1397
2. Camacho SVV, Schellart ANA, Shucksmith JD (2019) Quantifying the impact of uncertainty within the longitudinal dispersion coefficient on concentration dynamics and regulatory compliance in rivers. Water Resour Res 55(5):4393–4409
3. Caroppi G, Västilä K, Järvelä J, Rowinski PM, Giugni M (2019) Turbulence at water-vegetation interface in open channel flow: Experiments with natural-like plant. Adv Water Resour 127:180–191
4. Chen X, Zhu DZ, Steffler PM (2017) Secondary currents induced mixing at channel confluences. Can J Civ Eng 44(12):1071–1083
5. De Serio F, Meftah MB, Mossa M, Termini D (2018) Experimental investigation on dispersion mechanisms in rigid and flexible vegetated beds. Adv Water Resour 120:98–113
6. Dupuis V, Proust S, Berni C, Paquier A (2017a) Compound channel flow with a longitudinal transition in hydraulic roughness over the floodplains. Environ Fluid Mech 17:903–928
7. Dupuis V, Proust S, Berni C, Paquier A (2017b) Mixing layer development in compound channel flows with submerged and emergent rigid vegetation over the floodplains. Experimental Fluids 58:30
8. Fu B, Horsburgh JS, Jakeman AJ, Gualtieri C, Arnold T, Marshall L, Green TR, Quinn NW, Volk M, Hunt RJ, Vezzaro L, Croke BFW, Jakeman JD, Snow W, Rashleigh B (2020) Modeling water quality in watersheds: from here to the next generation. Water Resour Res 56:e2020WR0277212
9. Gabreil E, Tait S, Shao S, & Nichols A (2018) SPHysics simulation of laboratory shallow free surface turbulent flows over a rough bed. Journal of Hydraulic Research 56(5):727–747
10. Ghisalberti M, Nepf H (2005) Mass transport in vegetated shear flows. Environ Fluid Mech 5:527–551
11. Guymer I, Spence K (2009) Laboratory study of transverse solute mixing during over-bank flows. *In Proc. Of 33rd IAHR Congress: Water Engineering for Sustainable Environment, Ottawa, Canada.*
12. Hirschowitz PM, James CS (2008) Transverse velocity distributions in channels with emergent bank vegetation. River Res Appl 25(9):1177–1192
13. Ikeda S, Kanazawa M (1996) Three – dimensional organised vortices above flexible water plants. J Hydraul Eng 122(11):634–640
14. Jordanova AA, James CS, Birkhead AL (2006) Practical estimation of flow resistance through emergent vegetation. Water Manage 159(3):173
15. Kumar P, Legge A, Gregory DA, Nichols A, Jensen H, Ebbens SJ, Zhao X (2022) 3D printable self-propelling sensors for the assessment of water quality via surface tension. JCIS Open 5:100044
16. Liu C, Yan C, Shan Y, Guo Y (2022) An exponential-based model for predicting velocity fields in partially vegetated channels. J Hydraul Res 60(6):864–879
17. Mejía-Morales MA, Mignot E, Paquier A, Sigaud D and Proust S (2021) Impact of the porosity of an urban block on the flood risk assessment: A laboratory experiment. Journal of Hydrology 602:126715
18. Meftah MB, Mossa M (2016a) A modified log-law of flow velocity distribution in partly obstructed open channels. Environ Fluid Mech 16:453–479
19. Meftah MB, Mossa M (2016b) Partially obstructed channel: Contraction ratio effect on the flow hydrodynamic structure and prediction of the transversal mean velocity profile. J Hydrol 542:87–100
20. Meftah MB, Mossa M, De Serio F, Nepf HM (2017) How vegetation in flows modifies the turbulent mixing and spreading of jets. Sci Rep 7:6587
21. Mekonnen MM, Hoekstra AY (2016) Four billion people facing severe water scarcity. Sci Adv 2(2):e1500323
22. Muraro F, Dolcetti G, Nichols A, Tait SJ, Horoshenkov KV (2021) Free-surface behaviour of shallow turbulent flows. J Hydraul Res 59(1):1–20
23. Nepf HM (1999) Drag, turbulence and diffusion in flow through emergent vegetation. Water Resour Res 35(2):479

24. Nepf HM (2012) Flow and transport in regions with aquatic vegetation. Annual Rev Fluid Mech 44:123–142
25. Nezu I, Onitsuka K (2002) Turbulent structures in partly vegetated open-channel flows with LDA and PIV measurements. J Hydraul Res 39(6):629–642
26. Nichols A, Rubinato M (2016) Remote sensing of environmental processes via low-cost 3D free-surface mapping. Proceedings of the 4th IHAR Europe Congress, Liege, Belgium, 27–29
27. Nichols A, Tait SJ, Horoshenkov KV, Shepherd SJ (2016) A model of the free surface dynamics of shallow turbulent flows. J Hydraul Res 54(5):516–526
28. Oki T, Kanae S (2006) Global hydrological cycles and world water resources. Science 313(5790):1068–1072
29. Poggi D, Porporato A, Ridolfi L, Albertson JD, Katul GG (2004) The effect of vegetation density on canopy sub-layer turbulence. Boundary Layer Meteorol 11(3):565
30. Proust S, Fernandes JJ, Leal JB, Rivière N, Peltier Y (2017) Mixing layer and coherent structures in compound channel flows: effects of transverse flows, velocity ratio and vertical confinement. Water Resour Res 53(4):3387–3406
31. Proust S, Berni C, Nikora VI (2022) Shallow mixing layers over hydraulically smooth bottom in a tilted open channel. J Fluid Mech 951:A17
32. Raupach MR, Finnigan JJ, Brunet Y (1996) Coherent eddies and turbulence in vegetation canopies: The mixing layer analogy. Boundary Layer Meteorol 78(3–4):351
33. Rominger JT, Nepf HM (2011) Flow adjustment and interior flow associated with a rectangular porous obstruction. J Fluid Mech 680:636–659
34. Rojas Arques S, Rubinato M, Nichols A, Shucksmith JD (2018) Cost effective measuring technique to simultaneously quantify 2D velocity fields and depth-averaged solute concentrations in shallow water flows. J Flow Meas Instrum 64:213–223
35. Rojas Arques S (2021) A study of transverse mixing in shallow flows within partially vegetated channels. PhD Thesis, University of Sheffield
36. Rubol S, Battiato I, de Barros PJ (2016) Vertical dispersion in vegetated shear flows. Water Resour Res 52:8066–8080
37. Rutherford JC (1994) River mixing. J. Wiley and Sons LTD, New York
38. Sharma H, Ahmad Z (2018) Enhancing transverse mixing in streams with submerged vanes. Environ Fluid Mech 18(3):661–681
39. Shiono K, Knight DW (1991) Turbulent open-channel flows with variable depth across the channel. J Fluid Mech 222:617–646
40. Sonnenwald F, Guymer I, & Stovin V (2019) A CFD-based mixing model for vegetated flows. Water Resources Research 55:2322–2347. https://doi.org/10.1029/2018WR023628
41. Tang X, Knight DW, Sterling M (2010) A general analytical model for lateral velocity distributions in vegetated channels. River Flow 2010. Bundesanstalt für Wasserbau, Braunschweig, Germany, pp 1323–1330
42. Tang X, Knight DW, Sterling M (2011) Analytical model for streamwise velocity in vegetated channels. Proc Institution Civil Eng – Eng Comput Mech 164(2):91–102
43. UN-Water (2018) Water scarcity. https://www.unwater.org/water-facts/scarcity/ (accessed 11.06.2021)
44. Vargas CAA (2020) ndnanfilter.m (https://www.mathworks.com/matlabcentral/fileexchange/20417-ndnanfilter-m), *MATLAB Central File Exchange. Retrieved March, 2026 1*
45. Vörösmarty CJ, Pamela G, Salisbury J, Lammers RB (2000) Global water resources: Vulnerability from climate change and population growth. Science 289(5477):284–288
46. West P (2016) Quantifying solute mixing across low velocity emergent real vegetation shear layers. PhD Thesis. University of Warwick, School of Engineering
47. West PO, Wallis SG, Sonnenwald FC, Hart JR, Stovin V, Guymer I (2021) Modelling transverse solute mixing across a vegetation generated shear layer. J Hydraul Res 59(4):621–636
48. White BL, Nepf HM (2007) Shear instability and coherent structures in shallow flow adjacent to a porous layer. J Fluid Mech 593:1–32
49. White BL, Nepf HM (2008) A vortex-based model of velocity and shear stress in a partially vegetated shallow channel. Water Resour Res 44(1):W01412
50. Xie Z, Lin B, Falconer RA, Nichols A, Tait SJ, Horoshenkov KV (2022) Large-eddy simulation of turbulent free-surface flow over a gravel bed. J Hydraul Res 60(2):205–219
51. Zong L, Nepf H (2010) Flow and deposition in and around a finite patch of vegetation. Geomorphology 116(3–4):363–372

Publisher's note Springer Nature remains neutral with regard to jurisdictional claims in published maps and institutional affiliations.

Authors and Affiliations

S. Rojas-Arques[1,2] · A. Nichols[2] · J. D. Shucksmith[2]

✉ A. Nichols
a.nichols@sheffield.ac.uk

[1] Mott MacDonald, Madrid, Spain

[2] The University of Sheffield, Sheffield, UK